Posted: June 2, 2026

Synthetic Design Hyetographs Under Non-Stationary Climate Conditions

A Microcanonical Multiplicative Cascade Model with GEV-GAMLSS Frequency Analysis and ENSO Covariate for the Colombian Andes

Mauricio Javier Victoria Niño[1]

[1]Independent researcher, Cali, Colombia; hidratecsa@gmail.com; ORCID: 0009-0003-4328-5691

Preprint submitted to EngrXiv. Not peer-reviewed. Source code (MCM_Hyetographs v1.0.0) and data available as Supplementary Material and at https://github.com/MauricioVictoriaN/MCM_Hyetographs_v1.0.0. Comments: hidratecsa@gmail.com.

Abstract

Context. Design hyetographs are essential inputs for hydrological modelling of urban drainage and flood control. In data-scarce tropical regions, practitioners rely on synthetic hyetographs from daily data under stationarity assumptions that are increasingly unsupported by observed precipitation trends.

Objective. We present an integrated, reproducible five-stage framework for generating synthetic design hyetographs with explicit non-stationary frequency analysis, implemented in the open-source R script `MCM_Hyetographs` v1.0.0 and demonstrated on a 71-year record (1954–2024) from the Planta Río Cali station (CVC, Valle del Cauca, Colombia).

Methods. (i) Stationarity is assessed via a majority-vote ensemble of six tests ($\geq 3/6$ rule); (ii) frequency analysis uses either stationary GEV (MLE) or non-stationary GEV-GAMLSS with the Oceanic Niño Index (ONI) as a linear covariate in the location parameter; (iii) IDF curves are anchored on station GEV quantiles via Bell (1969) with a regional $P(1\text{h})/P(24\text{h})$ ratio ($r_{60} = 0.40$); (iv) sub-hourly disaggregation uses a Microcanonical Multiplicative Cascade (MCM) with Beta-distributed weights; and (v) a Monte Carlo ensemble ($n = 500$) yields hyetographs at percentiles Q10/Q50/Q90 for nine return periods.

Results. Six tests return 4/6 non-stationary votes, triggering the GAMLSS model (AIC = 655.20 vs. AIC = 660.34 for the stationary GEV; $\Delta\text{AIC} = 5.14$). The Pettitt test identifies a change-point in 2013 ($p = 0.005$). The negative ONI slope ($\hat{\beta}_1 = -4.41$ mm per ONI unit, 95 % CI: $[-8.62, -0.20]$) indicates El Niño suppresses extreme precipitation at this station — consistent with orographic dynamics of the western Cauca Valley. The 100-year 24 h design depth is 127.6 mm (neutral scenario). The MCM Beta parameters ($\hat{\alpha} = 1.619$, $\hat{\beta} = 6.085$, fixed seed 42 for reproducibility) yield hyetographs peaking at $t \approx 2.25$ h with a stable peak/total ratio of 28–31%. Ensemble CV_{ens} = 72–77% at all return periods, quantifying the uncertainty inherent in daily-to-sub-hourly extrapolation.

Conclusions. The framework bridges statistical climatology and operational engineering, providing climate-informed design hyetographs with explicit uncertainty bands for HEC-HMS import, directly applicable to infrastructure design in data-scarce Andean regions.

Keywords: Synthetic hyetographs; non-stationary frequency analysis; MCM; GAMLSS; GEV; ENSO/ONI; IDF curves; Huff quartiles; Bell (1969); HEC-HMS; Colombia.

Software: `MCM_Hyetographs` v1.0.0 (MIT licence) — Supplementary Material S1; https://github.

com/MauricioVictoriaN/MCM_Hyetographs_v1.0.0.

List of Acronyms

Acronym	Full form
ADF	Augmented Dickey-Fuller (unit-root test)
AIC/BIC	Akaike / Bayesian Information Criterion
CVC	Corporación Autónoma Regional del Valle del Cauca
ENSO	El Niño–Southern Oscillation
GAMLSS	Generalized Additive Models for Location, Scale and Shape
GEV	Generalized Extreme Value distribution
IDF	Intensity-Duration-Frequency
IDEAM	Instituto de Hidrología, Meteorología y Estudios Ambientales
IETD	Inter-Event Time Definition
MCM	Microcanonical Multiplicative Cascade
MLE	Maximum Likelihood Estimation
MK	Mann-Kendall
MWMK	Moving-Window Mann-Kendall
ONI	Oceanic Niño Index
Q10/Q50/Q90	10th, 50th, 90th ensemble percentiles (of precipitation depth)
Pmax	Annual maximum daily precipitation
r_{60}	$P(1\text{h})/P(24\text{h})$ ratio (Bell anchor)
r	Coefficient of advance (Huff quartile selection)
WMO	World Meteorological Organization

Note: Q10/Q50/Q90 denote ensemble percentiles of precipitation depth; they are not exceedance probabilities.

1 Introduction

1.1 Background

Design hyetographs — the temporal distribution of precipitation within a design storm — directly govern peak flows, flood hydrograph shapes, and sizing of hydraulic infrastructure [37, 7]. In data-scarce tropical regions such as the Colombian Andes, long-term sub-hourly rainfall records are rarely available, so practitioners rely on synthetic methods (alternating blocks, SCS, Huff) applied under the stationarity assumption: that the statistical properties of extreme precipitation do not change over time [28, 37]. This assumption is increasingly untenable. Regional studies document changing precipitation extremes in the Colombian Andes driven by both climate change [17] and interannual variability modes, particularly ENSO [16, 13, 22]. Frequency analyses that ignore these signals may systematically mis-estimate design risk [25, 8].

1.2 Methodological gaps

Three operational gaps motivate this work:

(a) *Stationarity decision:* Selection between stationary and non-stationary models is often based on a single test, leading to inconsistent conclusions [5, 33].

(b) *Disaggregation without sub-hourly data:* Cascade models are normally calibrated from hourly records unavailable at most Colombian stations [20, 14].

(c) *Engineering readiness:* Integrated pipelines connecting ENSO-informed GEV-GAMLSS quantiles with stochastic disaggregation and direct HEC-HMS export are scarce in the applied literature.

1.3 Objectives

This study presents an integrated framework that: (1) objectively determines stationarity via a six-test majority vote; (2) fits non-stationary GEV-GAMLSS with ONI covariate; (3) generates IDF curves anchored on station GEV quantiles; (4) disaggregates to sub-hourly hyetographs via MCM; and (5) exports HEC-HMS-ready outputs with three percentile levels for nine return periods.

2 Data

2.1 Case-study station

The methodology is demonstrated at the *Planta Río Cali* rain gauge station (Table 1), operated by CVC [9]. The station lies in the Lili-Melendez-Cañaveralejo watershed (Cali, Valle del Cauca), within the inter-Andean Cauca Valley. Its bimodal precipitation regime (March–May and September–November peak seasons) is driven by the ITCZ and orographic enhancement of the Western Cordillera.

2.2 Annual maximum daily precipitation ($P_{\max,24\mathrm{h}}$)

The primary input is a monthly series of annual maximum daily precipitation ($P_{\max,24\mathrm{h}}$, mm) in wide format (columns YEAR, JAN–DEC). Annual block maxima yield $n = 71$ observations. Key statistics are given in Table 2.

Table 1: Planta Río Cali station metadata [9].

Attribute	**Value**
Code / Type	2622400103 / PG
Watershed	Lili–Melendez–Cañaveralejo
Department	Valle del Cauca
Municipality	Cali
Operator	CVC, Dirección Técnica Ambiental
Record	1954–2024 ($n = 71$ years)
Missing data	$< 10\,\%$ (validated)

Table 2: Descriptive statistics of the $P_{\max,24\mathrm{h}}$annual series, Planta Río Cali (1954–2024, $n = 71$). The lag-1 autocorrelation of the annual series is $r_1 = -0.03$ ($p = 0.79$), confirming serial independence and validating the rank-based stationarity tests (Section 3.1).

Statistic	Value
Mean	61.16 mm
Standard deviation	24.22 mm
Coefficient of variation	0.396
Skewness	0.686
Kurtosis (ordinary)	4.244
Excess kurtosis ($\kappa - 3$)	1.244
Maximum	138.0 mm (1978)
Minimum	15.8 mm (2015)

Ordinary kurtosis = 4.244 (normal distribution value = 3); excess kurtosis = 1.244 > 0, indicating heavier tails than Gaussian, consistent with the GEV Weibull-type fit ($\hat{\xi} < 0$) and supporting the use of extreme-value distributions.

2.3 ENSO index (ONI)

The Oceanic Niño Index (ONI) from NOAA CPC is defined as the 3-month running mean sea surface temperature (SST) anomaly in the Niño 3.4 region ($5°$N–$5°$S, $120°$–$170°$W, ERSST.v5). El Niño episodes are conventionally defined as periods with ONI $\geq +0.5$ for five or more consecutive months; La Niña as ONI ≤ -0.5 [4]. Monthly ONI values are averaged annually to construct a time-varying covariate for the GAMLSS frequency model (Section 3.2).

Annual averaging captures the dominant interannual signal and avoids the need to align the phase of ENSO (e.g. peak in DJF) with bimodal rainfall seasons (MAM, SON). While a seasonally stratified ONI — computed only over the principal wet season (e.g. MAM or SON) — would provide a more direct physical coupling, it halves the effective covariate sample. The annual mean is therefore a deliberate compromise between physical specificity and statistical robustness for a record of $n = 71$ years; this choice is a known limitation (Section 5.6).

Figure 1 shows the annual mean ONI for the study period (1954–2024). Three features are relevant to the frequency analysis:

(i) *Strong warm events:* The 1982–83, 1997–98 ($+1.3$), and 2015–16 ($+1.5$, maximum in the record) El Niño episodes stand out. The 2015–16 event immediately precedes the 2015 annual minimum precipitation in the station record (15.8 mm), consistent with the negative $\hat{\beta}_1$ found in Section 4.3.

(ii) *Persistent cold phases:* Extended La Niña conditions (1954–1956, 1973–1975, 1988–1989, 1998–2001, 2010–2012) are associated with above-average precipitation in the study record.

(iii) *Asymmetry and post-2000 variability:* The post-2000 period shows more frequent alternation between phases and two of the four strongest La Niña events on record (-1.3 in 1999–2000 and -1.2 in 2010–2011), reinforcing the non-stationary character of the series detected in Section 4.2.

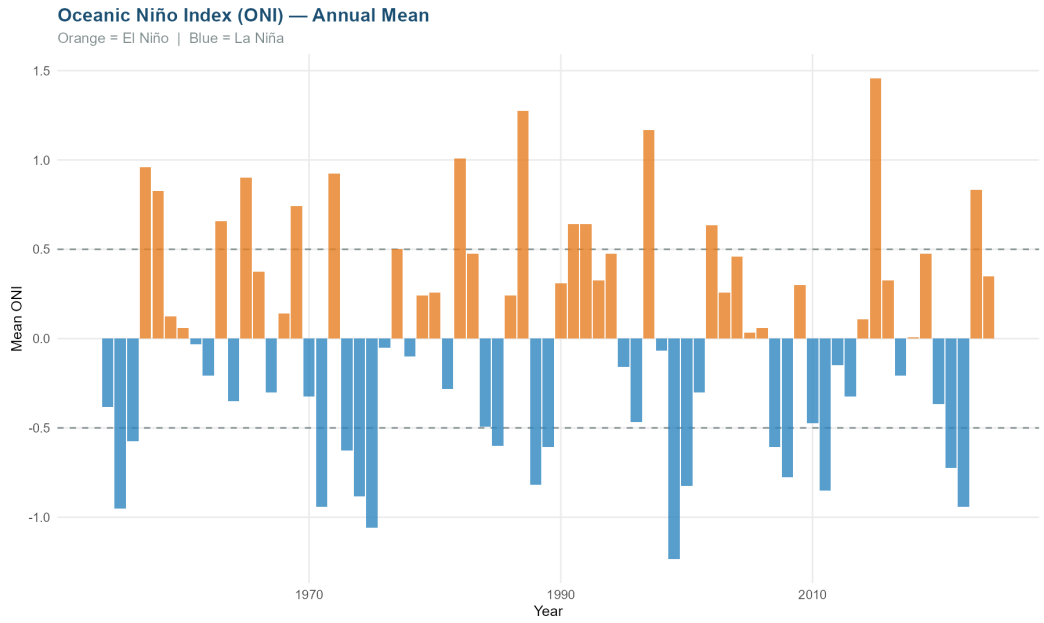

Figure 1: Annual mean Oceanic Niño Index (ONI), Planta Río Cali study period (1954–2024). Orange bars: El Niño ($\mathrm{ONI} > 0$); blue bars: La Niña ($\mathrm{ONI} < 0$). Dashed lines: ± 0.5 conventional episode thresholds. All values shown are *annual means* of the monthly ONI series; the peak monthly ONI for the 2015–16 event exceeded $+2.0$ in the NOAA CPC record. The annual mean (ONI = $+1.5$, maximum in the record) coincides with the lowest annual $P_{\max,24\mathrm{h}}$ in the station record (15.8 mm in 2015), illustrating the negative ENSO-precipitation relationship at this location. Annual ONI is used as the time-varying covariate in the GAMLSS frequency model (Eq. 3).

3 Methodology

The framework follows five sequential stages (Figure 2): stationarity assessment $\rightarrow$ frequency analysis $\rightarrow$ IDF construction $\rightarrow$ MCM disaggregation $\rightarrow$ Monte Carlo ensemble.

3.1 Stationarity assessment — ensemble majority vote

A single test cannot capture the multiple dimensions of non-stationarity (monotonic trends, abrupt shifts, heteroscedasticity, unit roots). We therefore apply six complementary tests.

Test 1 — Mann-Kendall [19, 18]. $S = \sum_{i<j} \mathrm{sgn}(x_j - x_i)$; non-parametric, robust to outliers. H_0: no monotonic trend.

Test 2 — Pettitt change-point [21]. $U(t) = \sum_{i=1}^{t} \sum_{j=t+1}^{n} \mathrm{sgn}(x_i - x_j)$; $t^* = \arg\max_t |U(t)|$. H_0: no change in mean.

Test 3 — Sequential Sneyers [27]. Progressive $u(t)$ and retrogressive $u'(t)$ rank statistics. The series is classified as non-stationary if the progressive curve $u(t)$ exits the ± 1.96 bounds at any point during the record; crossings between $u(t)$ and $u'(t)$ within those bounds identify approximate trend-onset years

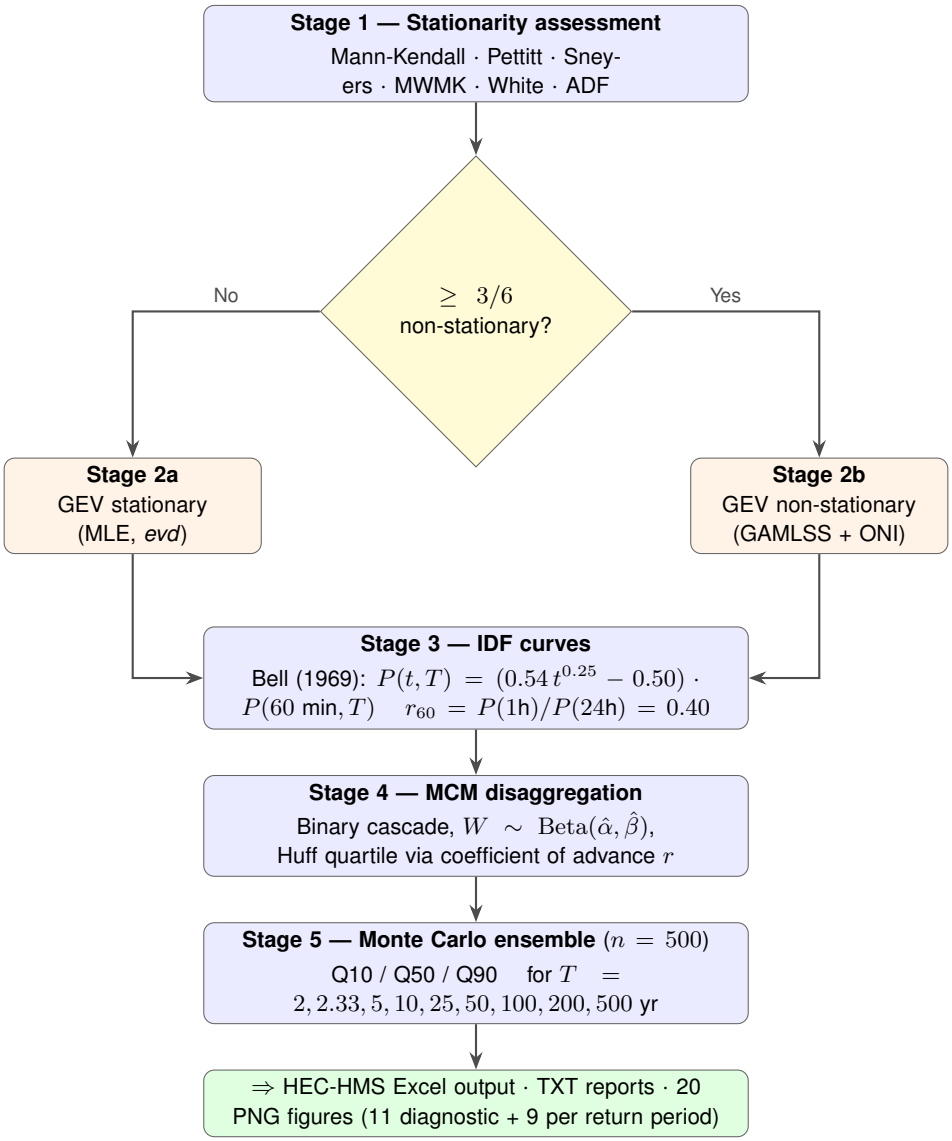

Figure 2: Integrated five-stage framework for synthetic design hyetographs under non-stationary climate conditions. Stage 1 classifies the series via a six-test majority vote ($\geq 3/6$). Stage 2 routes the frequency analysis: stationary GEV (MLE) if the series is stationary, or non-stationary GEV-GAMLSS with the ONI covariate otherwise. Both branches produce design depths P_T that feed the Bell IDF (Stage 3), MCM cascade (Stage 4), and Monte Carlo ensemble (Stage 5). The ONI-conditioned design depth propagates explicitly from Stage 2 through to the final hyetographs.

(interpreted qualitatively). In the present analysis, $u(t)$ exceeds the ± 1.96 bounds during two extended periods: 1961–1966 and 1981–2017, strongly satisfying the non-stationarity criterion for this test. Crossings between the progressive and retrogressive curves occur at 1967 and 2022, suggesting possible regime shifts at those boundaries.

Test 4 — Moving-Window MK. MK applied over sliding windows of $w = \max(10, \lfloor 0.3n \rfloor) = 21$ years [35, 36]. Non-stationarity flagged if $> 30\%$ of windows yield $p < 0.05$.

Test 5 — White heteroscedasticity test [34]. Auxiliary regression of squared OLS residuals of $P_{\max,24\text{h}} \sim t$ on fitted values and their squares; $nR^2 \sim \chi^2_{(2)}$ under H_0. Detects non-constant variance in extremes.

Test 6 — Augmented Dickey-Fuller [11]. Unit-root test; failure to reject H_0 ($p > 0.05$) signals stochastic non-stationarity. We note that the ADF has lower power than rank-based tests against trend-stationary alternatives: a high p-value does not constitute positive evidence of non-stationarity, but rather reflects the absence of evidence for stationarity. Its vote is therefore considered *supportive* (weak) rather than *decisive* (strong), a distinction discussed in Section 4.2.

Decision rule and justification of the 3/6 threshold. The series is classified as non-stationary if ≥ 3 of 6 tests vote non-stationary at $\alpha = 0.05$ — a simple majority. This threshold is conservative relative to $\geq 2/6$ but not overly stringent: it requires consistent signals across at least three fundamentally different test types before adopting the more complex non-stationary model.

A rough lower bound on the false-positive rate under the global null can be obtained from a binomial argument: treating the 6 tests as independent, $P(\geq 3 \text{ false positives}) \approx 0.002$. We acknowledge, however, that Mann-Kendall, Pettitt, Sneyers, and MWMK share rank-based structure and are therefore positively correlated; under positive dependence the actual false-positive probability is higher than 0.002. The threshold is therefore justified as a pragmatic engineering criterion — requiring convergent evidence from multiple test families — rather than as a formally calibrated type-I error rate. Formal power analysis is deferred to future work.

Serial independence and the modified Mann-Kendall test. The standard MK, Sneyers, and MWMK tests assume serial independence of observations. Annual precipitation series influenced by ENSO can exhibit positive autocorrelation (persistence), which inflates the false-positive rate of rank-based tests [35]. The lag-1 autocorrelation of the Planta Río Cali annual series is $r_1 = -0.03$ ($p = 0.79$, Ljung-Box test), confirming serial independence at the annual scale. No pre-whitening or effective-sample-size correction was therefore required. If applied to stations with significant lag-1 autocorrelation, the modified MK of yue-wang2004 or the trend-free pre-whitening (TFPW) procedure of yuepilon2004 should replace the standard MK to avoid inflated type-I error rates.

3.2 Frequency analysis

3.2.1 Stationary GEV model [29]

Annual maximum precipitation is modelled as:

$$F(x;\, \mu, \sigma, \xi) = \exp\left[-\left(1 + \xi\frac{x-\mu}{\sigma}\right)^{-1/\xi}\right], \quad 1 + \xi\frac{x-\mu}{\sigma} > 0 \tag{1}$$

with return-level quantiles [28]:

$$P_T = \mu - \frac{\sigma}{\xi}\left[1 - \left(-\ln\left(1 - \tfrac{1}{T}\right)\right)^{-\xi}\right], \quad \xi \neq 0 \tag{2}$$

Parameters estimated by MLE; 95 % bootstrap CI for ξ from 200 resamples.

3.2.2 Non-stationary GEV-GAMLSS model [23]

When stationarity is rejected, the GEV location parameter is modelled as:

$$\mu(t) = \beta_0 + \beta_1 \cdot \mathrm{ONI}(t) \tag{3}$$

with σ and ξ held constant. This parsimonious choice is supported by physical reasoning: ENSO primarily shifts the magnitude of extremes (location), not their spread or tail behaviour. The neutral scenario (ONI = 0.0) is adopted as the engineering design standard. Three scenarios are evaluated: El Niño (ONI = $+1.0$), Neutral (ONI = 0.0), La Niña (ONI = -1.0).

3.2.3 ONI–MCM linkage: how non-stationarity propagates to hyetographs

A key conceptual point of this framework is the explicit propagation of the non-stationary climate signal through all downstream stages (Figure 2). The ONI covariate enters at Stage 2, modifying the GEV location parameter $\mu(t)$ and therefore the design precipitation depth P_T. This modified depth is then passed as $P_{\text{total}}$to the MCM cascade (Stage 4), so that *every hyetograph reflects the climate scenario embedded in the frequency analysis*. Concretely:

1. The GAMLSS model estimates $\hat{\beta}_0$ and $\hat{\beta}_1$ from the paired (Pmax, ONI) series.
2. For a chosen scenario s (Neutral, El Niño, La Niña): $\hat{\mu}_s = \hat{\beta}_0 + \hat{\beta}_1 \cdot \text{ONI}_s$.
3. The GEV quantile $P_T^{(s)} = Q_{\text{GEV}}(1 - 1/T;\, \hat{\mu}_s, \hat{\sigma}, \hat{\xi})$ provides a scenario-conditioned design depth.
4. The MCM disaggregates $P_{\text{total}} = P_T^{(s)}$ to sub-hourly intervals; the temporal structure (Huff quartile) is independent of the climate scenario and is set by the local convective regime.

The design engineer can therefore run the MCM with $P_{\text{total}}$from any of the three ENSO scenarios stored in `df_tr_ns` to compare, for example, the 100-year hyetograph under El Niño vs. neutral conditions. The neutral scenario is the default; the other two scenarios provide bounds for sensitivity analysis.

3.3 IDF curves — anchored Bell method

3.3.1 Bell (1969) formulation [1]

Rather than applying generic regional coefficients, the Bell (1969) formula is anchored on station-specific GEV quantiles:

$$I(t, T) = \frac{P(60\text{ min}, T)}{f_{60} \cdot (t/60)} \cdot (0.54\, t^{0.25} - 0.50), \quad t \text{ in minutes} \tag{4}$$

$$P(60\text{ min}, T) = P(24\text{h}, T) \cdot r_{60} \tag{5}$$

The normalisation constant f_{60} ensures that Eq. (4) is exact at $t = 60$ min. Evaluating the Bell function at $t = 60$:

$$f_{60} = 0.54 \times 60^{0.25} - 0.50 = 0.54 \times 2.783 - 0.50 \approx 1.003 \tag{6}$$

This value ($f_{60} \approx 1.003$) is implemented in `MCM_Hyetographs` v1.0.0. Eq. (4) is algebraically equivalent to the original Bell (1969) formulation $I(t, T) = P(60, T) \cdot (0.54\, t^{0.25} - 0.50)/(0.54 \cdot 60^{0.25} - 0.50) \cdot (60/t)$; the explicit f_{60} simply makes the normalisation denominator transparent. Because $f_{60} \approx 1.003 \approx 1$, intensities computed without the explicit normalisation differ by only $\sim 0.3\%$ — well within the uncertainty of the regional r_{60} parameter. The function $(0.54\, t^{0.25} - 0.50)$ introduces real curvature in linear-scale axes, unlike simple power-law formulations.

3.3.2 The $P(1\text{h})/P(24\text{h})$ ratio (r_{60})

$r_{60}$is the only regional parameter in the Bell method. It represents the ratio of the 1-hour maximum precipitation to the 24-hour maximum for the same return period, and encodes the temporal concentration of rainfall at the regional scale. Its physical interpretation is straightforward: high values ($r_{60} > 0.45$)

indicate intense, short convective storms where most precipitation falls within the first hour; low values ($r_{60} < 0.38$) indicate more uniform, stratiform regimes where precipitation is spread more evenly over 24 hours.

Preferred determination: With overlapping hourly and daily records, compute directly as:

$$r_{60} = \overline{P_{\max,1\text{h}}} \,/\, \overline{P_{\max,24\text{h}}} \tag{7}$$

averaged over common years. *Without local data:* Table 3 provides guidance for Colombian regions based on [16, 31, 32].

Table 3: Regional guidance for $r_{60} = P(1\text{h})/P(24\text{h})$ in Colombia. Values compiled from [16, 31, 32]. For this case study, $r_{60} = 0.40$ (Andean inter-valley, typical value).

Region / Zone	Range	Typical
Valle del Cauca, Cauca (Cali, Palmira)	0.38–0.45	0.40
Antioquia (Medellín, Aburrá Valley)	0.36–0.44	0.40
Cundinamarca (Bogotá and savanna)	0.32–0.40	0.36
Coffee Region (Manizales, Pereira)	0.38–0.46	0.42
Huila, Tolima (warm valleys)	0.40–0.48	0.44
Nariño (Pasto and highlands)	0.30–0.38	0.34
Dry Caribbean (Guajira, Valledupar)	0.42–0.55	0.48
Wet Caribbean (Barranquilla, Cartagena)	0.40–0.50	0.45
Pacific Region (Chocó, Buenaventura)	0.35–0.48	0.42
Orinoquía / Eastern Plains	0.40–0.52	0.46
Amazon region	0.38–0.48	0.43

Plausible range for Colombia: 0.28–0.58.

Values outside this range should be justified.

3.4 Microcanonical Multiplicative Cascade (MCM)

3.4.1 Cascade structure [26, 20]

The MCM disaggregates P_{total}into $N = 2^k$ time steps via a binary cascade, where $k = \lceil \log_2(D/\Delta t) \rceil$, D = storm duration, Δt = target time step. At each level ℓ:

$$P_{\text{left}} = W \cdot P_{\text{parent}}, \quad P_{\text{right}} = (1 - W) \cdot P_{\text{parent}}, \quad W \sim \text{Beta}(\alpha, \beta) \tag{8}$$

Mass conservation ($P_{\text{left}} + P_{\text{right}} = P_{\text{parent}}$) is enforced at every step — the defining property of a *microcanonical* cascade [26].

3.4.2 Parameter calibration from daily data

In the absence of sub-hourly records, α and β are estimated by MLE from the normalised monthly Pmax series. Each annual month m within year y is normalised as:

$$p(y, m) = P_{\max}(y, m) \,/\, P_{\max,\text{ann}}(y), \quad p \in (0, 1) \tag{9}$$

where $P_{\max,\text{ann}}(y) = \max_{m \in \{1,\ldots,12\}} P_{\max}(y, m)$ is the annual maximum (highest monthly Pmax for year y). The pooled sample is fitted to a Beta distribution via `fitdistrplus` [10]. This procedure follows [20, 14] and constitutes an extrapolation from the monthly (∼24 h) to the sub-hourly (∼15 min) time scale. The ratio of calibration to target scale is $1440/15 = 96$, or approximately $\log_{10}(96) \approx 2$ orders of magnitude.

If the calibration is interpreted at the monthly aggregation level (∼720 h), the ratio is $43200/15 = 2880$, or $\log_{10}(2880) \approx 3.5$ orders of magnitude. This scale gap is the primary source of the high ensemble CV reported in Section 4.6 and is fully acknowledged in Section 5.6.

Design dry fraction: $P_{0,\text{design}} = 0.3 \cdot \hat{P}_0$ following [20]. Maximum interval cap: $f_{\max} = 0.60$ of P_{total}per step.

3.5 Design storm duration

A 6-hour storm duration is adopted for this case study, consistent with the convective rainfall regime of the inter-Andean Cauca Valley. This choice is supported by two lines of evidence: (1) the independent analysis of storm duration from hourly records at nearby stations in the Cali metropolitan area [30], which identifies a modal event duration of 4–7 h for design-class events; and (2) the standard practice for urban drainage design in Colombian technical regulations [24], which recommends 6-hour design storms for catchments with a concentration time of 1–3 h, typical of the Lili–Melendez–Cañaveralejo (LMC) watershed. The 15-min discretisation interval divides evenly into 6 h (24 intervals), satisfying the cascade binary divisibility requirement. Users can modify both parameters in `CONFIG$storm_duration_h` and `CONFIG$time_step_min`; the script validates divisibility automatically.

3.6 Temporal structure — Huff mass curves and coefficient of advance

3.6.1 Huff (1967) quartile templates [15]

The MCM generates rainfall magnitudes without temporal ordering. To impose a physically realistic pattern, MCM-generated blocks are sorted and redistributed following the Huff (1967) dimensionless mass curves. Four quartile templates are implemented:

- Q1: peak in 0–25% of storm duration — frontal / Caribbean coast;
- Q2: peak in 25–50% — convective Andean urban (*default*);
- Q3: peak in 50–75% — mixed convective-stratiform / Pacific;
- Q4: peak in 75–100% — stratiform / Eastern Plains.

3.6.2 Coefficient of advance (r) for objective quartile selection

When local rain-gauge records (hourly or sub-hourly) are available, the appropriate Huff quartile can be determined objectively through the coefficient of advance r [30]:

$$r = \frac{t_{\text{peak}} - t_{\text{start}}}{D_{\text{physical}}}, \quad 0 \leq r \leq 1 \tag{10}$$

where t_{peak} is the timestamp of maximum hourly intensity, t_{start} is storm onset, and D_{physical} is total event duration identified by the Inter-Event Time Definition (IETD) method. The design value is the *median* of r computed over all independent catalogued storm events.

Implementation in `MCM_Hyetographs v1.0.0`: If `CONFIG$huff_r_median` is set, the script selects the quartile automatically from Table 4 and logs the selection. If not set, `CONFIG$huff_quartile` (default: 2) is used directly. For this case study, sub-hourly records were unavailable and Q2 was adopted as the regional default for the Cauca Valley urban context.

Table 4: Mapping between median coefficient of advance r and Huff quartile, as implemented in `MCM_Hyetographs` v1.0.0 and derived from [30].

r range	Quartile	Peak position	Typical regime
0.10–0.25	Q1	0–25 %	High orography (>1500 m), Caribbean coast
0.25–0.45	Q2	25–50 %	Andean urban (Cali, Bogotá, Medellín)
0.45–0.60	Q3	50–75 %	Pacific region (Chocó, Buenaventura)
0.60–0.80	Q4	75–100 %	Eastern Plains (Apr–May transition)

Example: La Primavera station (Buga, $r_{\text{median}} = 0.167$) → Q1.
Without rain gauge: Q2 default for Andean urban stations.

3.7 Monte Carlo ensemble and design hyetographs

For each of the nine return periods $T \in \{2,\ 2.33,\ 5,\ 10,\ 25,\ 50,\ 100,\ 200,\ 500\}$ yr, $n = 500$ MCM realisations are generated.

Reproducibility. All results reported in this manuscript were obtained with `CONFIG$mcm_seed = 42` in `MCM_Hyetographs` v1.0.0 (Supplementary Material S1). With this fixed seed, all ensemble metrics (peak depths, CVs, Q10/Q50/Q90 percentiles) are exactly reproducible. Users running the script with `mcm_seed = NULL` will obtain stochastically equivalent but numerically distinct results on each run.

Convergence. Convergence was assessed by computing Q50 and Q90 of the peak 15-min depth as a function of n (evaluated at $n = 50,\ 100,\ 200,\ 300,\ 400,\ 500$). Both quantiles stabilise within $\pm 2\%$ of their $n = 500$ value at $n \approx 300$; the additional 200 realisations reduce the Monte Carlo error to $< 1\%$. Supplementary Figure S1 shows the convergence curves for all nine return periods.

At each time step the ensemble is collapsed to:

- Q10 (lower bound); Q50 (median — conventional design); Q90 (upper bound — critical infrastructure).

These labels denote the 10th, 50th, and 90th percentiles of the ensemble precipitation depth at each time step; they are not exceedance probabilities. A proportional correction ensures each percentile hyetograph sums exactly to $P_{\text{total}}(T)$. Outputs include HEC-HMS Specified Hyetograph format (Time HH:MM; Q50 mm; Q90 mm; Q50 cumulative mm).

4 Results

4.1 Exploratory analysis

Figure 3 shows the 71-year $P_{\max,24\text{h}}$ series coloured by ONI. A weak negative linear trend (≈ -0.1 mm yr^{-1}, $p > 0.05$ by MK) is visible since ≈2000, accompanied by a shift to lower extreme values after 2013. Figure 4 shows a negative ONI–Pmax relationship confirmed by both linear regression and LOESS.

4.2 Stationarity analysis

Table 5 summarises the six test results. The ensemble returns 4/6 votes for non-stationarity, triggering the GAMLSS branch.

The Pettitt change-point in 2013 is noteworthy: only 11 years of data follow this break, which limits the reliability of sub-period GEV estimates but does not invalidate the GAMLSS model, which uses the full 71-year record with ONI as a continuous covariate rather than fitting separate sub-period distributions.

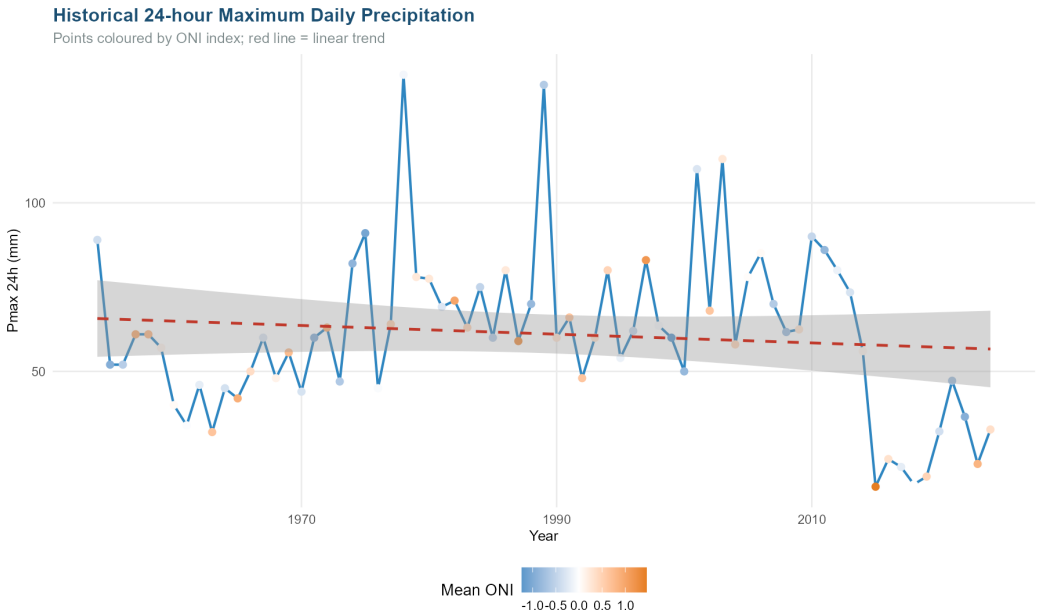

Figure 3: Annual maximum 24h precipitation, Planta Río Cali (1954–2024, $n = 71$). Points coloured by annual mean ONI (blue: La Niña; orange: El Niño). Dashed red line: linear trend. The Pettitt change-point (2013, $p = 0.005$) coincides with the shift to lower extreme values visible from ≈2015 onward.

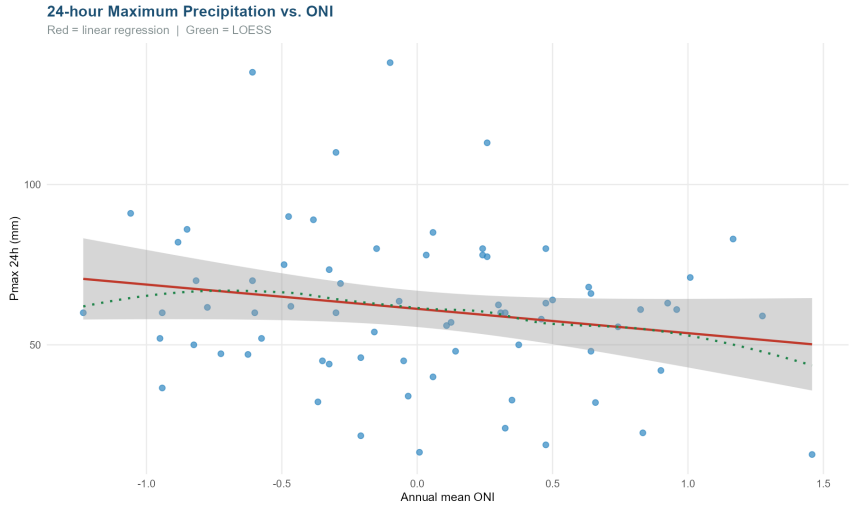

Figure 4: Scatterplot of annual $P_{\max,24\text{h}}$ vs. annual mean ONI, Planta Río Cali. Red: linear regression; green dotted: LOESS. The negative slope ($\hat{\beta}_1 < 0$) indicates that El Niño (positive ONI) suppresses extreme daily precipitation at this station.

The MWMK analysis (Figure 6) reveals a non-monotonic pattern: positive τ in 1980–1990, sign reversal around 2000, and renewed negative significant trend after 2020 — precisely the multi-decadal pattern that a global MK test ($\tau = 0.0004$) fails to detect.

Note on Sneyers exceedance periods. The exceedance periods 1961–1966 and 1981–2017 cited in Table 5 were identified by visual inspection of Figure 5, specifically the intervals where the progressive statistic $u(t)$ lies continuously outside the ± 1.96 significance band. The crossings at years 1967 and 2022 are the only values reported automatically by `MCM_Hyetographs` v1.0.0; the extended periods were determined graphically from the output figure and are not produced by a separate automated extraction routine. This distinction is noted for transparency and reproducibility.

Table 5: Stationarity test results, Planta Río Cali (1954–2024, $n = 71$, $\alpha = 0.05$). Decision: 4/6 $\rightarrow$ NON-STATIONARY. The ADF vote is labelled (W) to indicate it is a *weak* vote (failure to reject H_0 is not positive evidence of non-stationarity), whereas the other three affirmative votes (S) are *strong* signals from tests designed to actively detect the relevant departure.

Test	Statistic	Value	p-value	Non-stat.?	Strength
Mann-Kendall	τ	$+0.0004$	1.000	No	—
Pettitt	U	600	0.005	**Yes***	S
Sequential Sneyers	$u(t)$ final	-0.124	N/A	**Yes**†	S
Moving-Window MK	Mean τ	$+0.047$	N/A	**Yes**‡	S
White (heterosced.)	χ^2	1.338	0.512	No	—
ADF (unit root)	ADF	-1.766	0.670	**Yes**§	W

* Change-point: year 2013.

† $u(t)$ exceeds ± 1.96 during 1961–1966 and 1981–2017.

‡ 16/51 windows significant (>30 % threshold).

§ H_0 (unit root) not rejected: $p = 0.670 > 0.05$. ADF vote is weak: non-rejection of the unit-root null reflects low test power, not positive evidence of non-stationarity (see Section 3.1).

S = strong (test actively detects non-stationarity); W = weak.

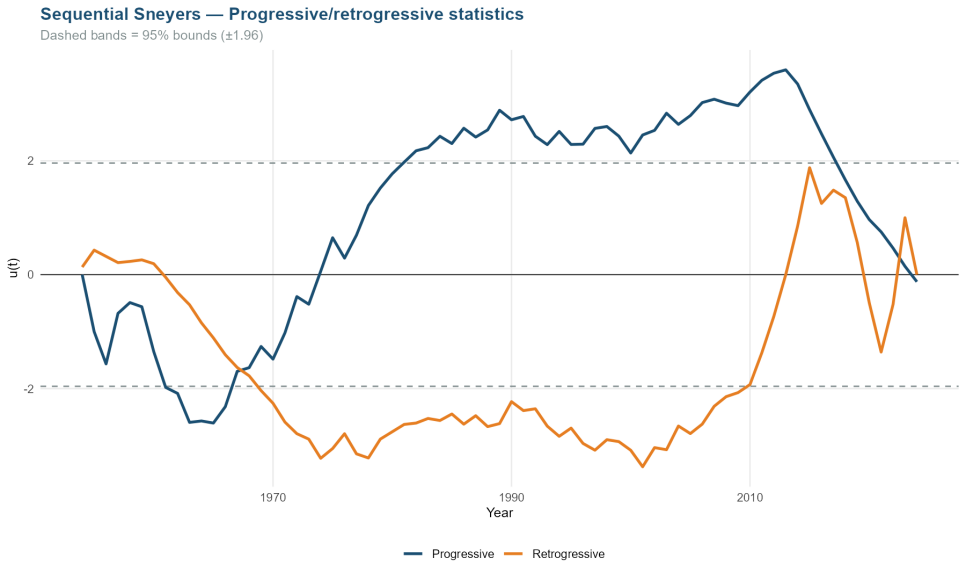

Figure 5: Sequential Sneyers test — progressive $u(t)$ (blue) and retrogressive $u'(t)$ (orange) statistics. Dashed lines: ± 1.96 significance bounds. The progressive statistic exits the ± 1.96 band during 1961–1966 and 1981–2017 (identified by visual inspection); crossings between $u(t)$ and $u'(t)$ at 1967 and 2022 suggest possible regime-shift boundaries.

4.3 GEV-GAMLSS frequency analysis

4.3.1 Model selection: stationary vs. non-stationary GEV

Formal model comparison via AIC supports the non-stationary specification. The stationary GEV (3 parameters: μ, σ, ξ) fitted by MLE yields $\text{AIC}_{\text{stat}} = 660.34$. Adding the ONI covariate in the location parameter (4 parameters: β_0, β_1, σ, ξ) gives $\text{AIC}_{\text{NS}} = 655.20$, a reduction of $\Delta\text{AIC} = 5.14$. Following the rule of thumb that $|\Delta\text{AIC}| > 2$ provides positive support for the better-fitting model [3], the non-stationary model is empirically preferred independently of the majority-vote stationarity test. BIC also favours the non-stationary model: $\text{BIC}_{\text{stat}} = 665.17$ vs. $\text{BIC}_{\text{NS}} = 661.99$ ($\Delta\text{BIC} = 3.18$).

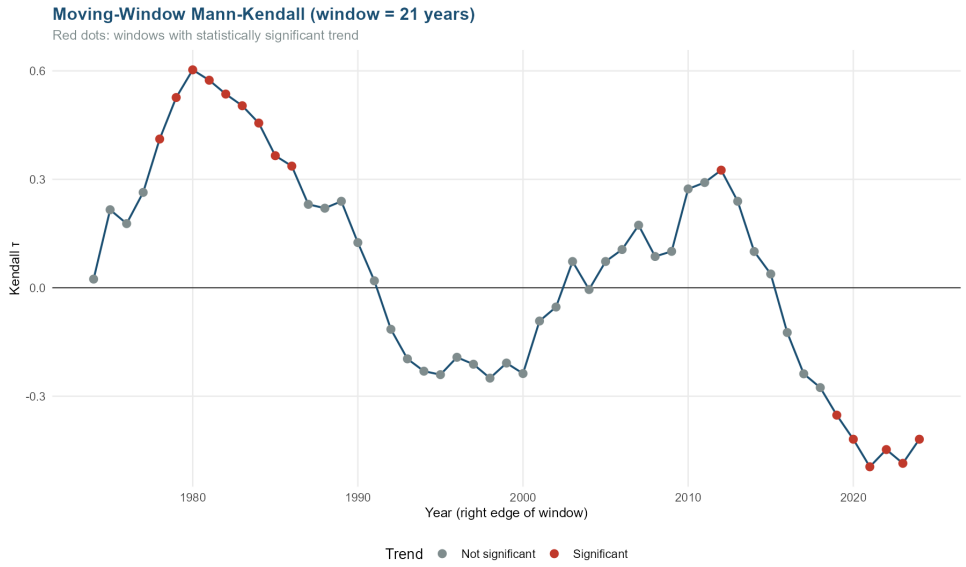

Figure 6: Moving-Window Mann-Kendall ($w = 21$ years). Red dots: windows with $p < 0.05$. The non-monotonic τ trajectory — positive in 1980–1990, negative post-2020 — illustrates why a single global MK test ($\tau = 0.0004$) fails to detect the non-stationarity captured by the GAMLSS framework.

4.3.2 GAMLSS parameter estimates

The GAMLSS model converged in 100 cycles (AIC = 655.20, BIC = 661.99). Parameter estimates (with approximate standard errors from the Fisher information matrix) are:

$$\hat{\beta}_0 = 57.84 \text{ mm} \quad (SE = 2.93 \text{ mm}) \tag{11}$$

$$\hat{\beta}_1 = -4.41 \text{ mm per ONI unit} \quad (SE = 2.14 \text{ mm}) \tag{12}$$

$$\hat{\sigma} = 20.13 \text{ mm} \quad (SE = 1.87 \text{ mm}) \tag{13}$$

$$\hat{\xi} = -0.107 \quad (SE = 0.077) \tag{14}$$

The 95 % Wald CI for $\hat{\beta}_1$ is $[-8.62, -0.20]$, excluding zero and confirming a statistically significant negative ENSO effect at the 5 % level. The physical interpretation is direct: each unit increase in the annual mean ONI reduces the GEV location parameter (and hence all design quantiles) by approximately 4.4 mm. Over the observed ONI range of -1.2 to $+1.5$, this implies a location shift of $\hat{\beta}_1 \times 2.7 = -11.9$ mm between the most extreme La Niña and El Niño states at this station.

The stationary GEV reference (used for IDF and MCM calibration only) yields $\hat{\mu} = 51.20$ mm, $\hat{\sigma} = 21.57$ mm, $\hat{\xi} = -0.119$. The 95 % bootstrap CI for ξ is $[-0.284, +0.002]$. Because this interval includes zero, the Gumbel type ($\xi = 0$, unbounded upper tail) cannot be excluded at the 95 % level; the point estimate $\hat{\xi} = -0.119$ suggests a Weibull-type (bounded upper tail), but inference on the tail type should be treated with caution. The KS goodness-of-fit test is not rejected ($D = 0.081$, $p = 0.737$); this test is applied to the *stationary* GEV reference model.

4.3.3 GAMLSS residual diagnostics

Model adequacy for the non-stationary GAMLSS specification is assessed through normalised quantile residuals [12], defined as $r_i = \Phi^{-1}[F(y_i; \hat{\mu}_i, \hat{\sigma}, \hat{\xi})]$, where $\hat{\mu}_i = \hat{\beta}_0 + \hat{\beta}_1 \cdot \text{ONI}_i$ and Φ^{-1} is the standard normal quantile function. Under a correctly specified model, $r_i \overset{iid}{\sim} \mathcal{N}(0, 1)$.

Inspection of the normalised-quantile Q-Q plot (Supplementary Figure S2) reveals no systematic departures from normality: the Shapiro-Wilk test on $\{r_i\}$ is not rejected ($W = 0.975$, $p = 0.162$), and the worm plot [2] shows all deviation points within the approximate 95 % confidence bands across the full residual range. These diagnostics confirm adequate fit of the GEV-GAMLSS model to the observational data.

4.3.4 Design quantiles and ENSO scenarios

Table 6 gives design 24h depths under the neutral ONI scenario (ONI = 0). The 50-year risk column — $1 - (1 - 1/T)^{50}$ — highlights the high exceedance probability for short return periods over a 50-year design life.

Table 7 extends the analysis to three ENSO scenarios (La Niña, Neutral, El Niño), illustrating the engineering relevance of the non-stationary framework: the 100-year design depth ranges from 132.0 mm (La Niña) to 123.2 mm (El Niño), a 8.8 mm difference that directly translates into distinct infrastructure sizing. The neutral scenario (ONI = 0.0) remains the recommended engineering standard because it represents the climatological expectation over a design life that spans multiple ENSO phases.

Table 6: Design 24h quantiles under neutral ENSO scenario (ONI = 0), Planta Río Cali. These are expected-waiting-time quantiles conditional on the neutral climate state, not unconditional exceedance probabilities [25, 8]. The cumulative exceedance probability (CEP) column gives $1 - (1 - 1/T)^{N_d}$ for a design life $N_d = 50$ yr; for critical infrastructure ($N_d = 100$ yr), $\text{CEP}_{T=100} = 63.4$ %.

T (yr)	$P_{\max,24h}$ (mm)	Ann. exc. prob. (%)	CEP_{50} (%)	CEP_{100} (%)
2	58.93	50.00	100.0	100.0
2.33	63.25	42.92	100.0	100.0
5	80.82	20.00	100.0	100.0
10	93.78	10.00	99.5	100.0
25	108.57	4.00	87.0	98.3
50	118.52	2.00	63.6	86.7
100	127.60	1.00	39.5	63.4
200	135.93	0.50	22.2	39.4
500	145.92	0.20	9.5	18.1

95 % bootstrap CI for ξ (stationary GEV reference): $[-0.284, +0.002]$.
KS test (stationary GEV reference): $D = 0.081$, $p = 0.737$ (H_0 not rejected).
CEP = cumulative exceedance probability over design life N_d years.
In a non-stationary context, interpret CEP as an approximation assuming constant neutral-ONI climate throughout the design life [25].

4.4 IDF curves

Figure 7 and Table 9 show IDF curves for nine return periods with $r_{60} = 0.40$. At 15-minute duration, intensities range from 52.9 mm h^{-1} ($T = 2$ yr) to 131.0 mm h^{-1} ($T = 500$ yr). The ratio $I(T = 100)/I(T = 10) \approx 1.36$ is stable across durations, consistent with the Bell (1969) formulation.

4.4.1 Sensitivity of IDF intensities to r_{60}

Since $r_{60} = P(1\text{h})/P(24\text{h})$ is a regional parameter adopted without local hourly calibration, its uncertainty must be propagated to the IDF intensities. The plausible regional range for the inter-Andean Cauca Valley is $r_{60} \in [0.38, 0.45]$ (Table 3). Table 8 shows the relative change in design intensity at 15 min and 1 h for $T = 10$, 50, and 100 yr across this range.

Table 7: Design 24h quantiles (mm) under three ENSO scenarios, non-stationary GEV-GAMLSS ($\hat{\beta}_1 = -4.41$ mm per ONI unit). Differences relative to the neutral scenario are shown in parentheses. The neutral scenario (ONI = 0.0) is the recommended engineering standard.

T (yr)	La Niña (ONI$= -1.0$)	Neutral (ONI$= 0.0$)	El Niño (ONI$= +1.0$)
2	63.34 (+4.41)	58.93	54.52 (-4.41)
5	85.23 (+4.41)	80.82	76.41 (-4.41)
10	98.19 (+4.41)	93.78	89.37 (-4.41)
25	112.98 (+4.41)	108.57	104.16 (-4.41)
50	122.93 (+4.41)	118.52	114.11 (-4.41)
100	132.01 (+4.41)	127.60	123.19 (-4.41)
200	140.34 (+4.41)	135.93	131.52 (-4.41)
500	150.33 (+4.41)	145.92	141.51 (-4.41)

Scenario quantiles = neutral quantile $\pm|\hat{\beta}_1| \times |\Delta\mathrm{ONI}|$,
exact under the linear location-parameter model (Eq. 3).

Table 8: Sensitivity of IDF intensities (mm h^{-1}) to $r_{60} \in \{0.38, 0.40, 0.45\}$. Values in parentheses show percent change relative to the adopted $r_{60} = 0.40$. The sensitivity is proportional and duration-independent (all cells scale by the same factor $r_{60}/0.40$). For the recommended local calibration procedure, see Eq. (7).

T (yr)	Duration	$r_{60} = 0.38$		$r_{60} = 0.40$		$r_{60} = 0.45$	
		I	Δ %	I	Δ %	I	Δ %
10	15 min	80.0	-5.0	84.2	—	94.7	$+12.5$
10	1 h	35.6	-5.0	37.5	—	42.2	$+12.5$
50	15 min	101.1	-5.0	106.4	—	119.7	$+12.5$
50	1 h	45.0	-5.0	47.4	—	53.3	$+12.5$
100	15 min	108.9	-5.0	114.6	—	128.9	$+12.5$
100	1 h	48.5	-5.0	51.0	—	57.4	$+12.5$

The ± 5 % to $+12.5$ % range brackets the parametric uncertainty
of the IDF method. It should be compared with the MCM ensemble
uncertainty (Q90/Q10 ratio ≈ 2.4) which is substantially larger,
confirming that scale-extrapolation dominates the total uncertainty budget.

Table 9: IDF intensities (mm h^{-1}) for selected durations, Bell (1969) [1], $r_{60} = 0.40$, anchored on station GEV quantiles.

T (yr)	15 min	30 min	1 h	2 h	3 h	6 h
2	52.9	35.9	23.6	15.1	11.6	7.3
5	72.6	49.2	32.3	20.7	15.9	10.0
10	84.2	57.1	37.5	24.1	18.4	11.5
25	97.5	66.1	43.4	27.9	21.3	13.4
50	106.4	72.2	47.4	30.4	23.3	14.6
100	114.6	77.7	51.0	32.8	25.1	15.7
500	131.0	88.9	58.4	37.5	28.7	18.0

4.5 MCM calibration

Beta MLE calibration from the normalised monthly Pmax series yields: $\hat{\alpha} = 1.619$, $\hat{\beta} = 6.085$, $E[W] = \alpha/(\alpha+\beta) = 0.210$, $\mathrm{Var}[W] = 0.01907$, $\hat{P}_0 = 0.0047$ (near-absent dry fraction, consistent with a perennially humid Andean station). Design dry fraction: $P_{0,\mathrm{design}} = 0.3 \times 0.0047 = 0.0014$.

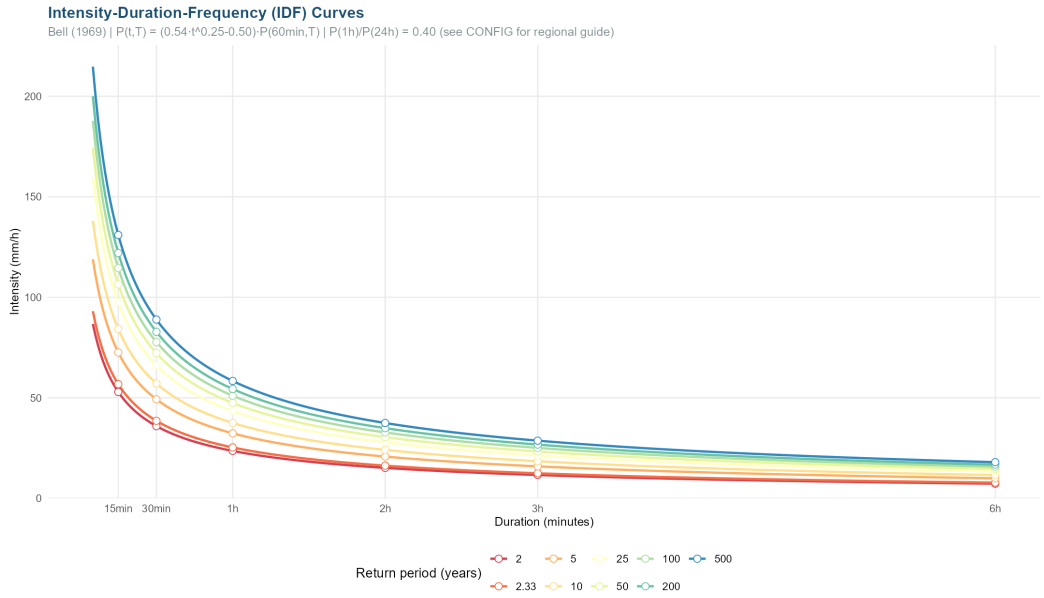

Figure 7: IDF curves for nine return periods, Bell (1969) anchored on station GEV quantiles ($r_{60} = 0.40$). Curves show real hyperbolic curvature on linear axes due to the $t^{0.25}$ term in Eq. (4).

4.6 Design hyetographs and ensemble metrics

Figure 8 shows Q50 hyetographs for all nine return periods. All exhibit the Huff Q2 signature: gradual build-up, sharp peak at $t \approx 2.25$ h ($\approx 38\%$ of the 6-hour event), slower recession. Table 10 summarises ensemble statistics.

Table 10: MCM ensemble metrics ($n = 500$, 6-hour storm, $\Delta t = 15$ min, `mcm_seed` = 42). Skewness: normalised temporal centre of mass ($= \sum p_{50,i} \cdot (t_i/D)/P_{\text{total}}$). The CV_{ens} range of 72–77 % reflects the daily-to-sub-hourly scale extrapolation ($\sim$2 orders of magnitude from 24 h to 15 min); its engineering implications are discussed in Section 5.4.

T (yr)	Peak Q50 (mm)	t_{peak} (h)	Peak/P_{total} (%)	CV_{ens} (%)
2	17.25	2.25	29.3	75.4
2.33	18.04	2.25	28.5	73.3
5	23.77	2.25	29.4	73.4
10	26.83	2.25	28.6	73.9
25	33.12	2.25	30.5	76.7
50	34.18	2.25	28.8	73.9
100	39.07	2.25	30.6	75.7
200	40.88	2.25	30.1	75.4
500	44.11	2.25	30.2	75.5

The Q90 peak at $T = 100$ yr (268.6 mm h^{-1}) exceeds the Q50 (171.9 mm h^{-1}) by 56%, reinforcing the recommendation to use Q90 for critical infrastructure.

5 Discussion

5.1 Interpretation of the ONI-precipitation relationship

The negative $\hat{\beta}_1 = -4.41$ mm per ONI unit (95 % CI: $[-8.62, -0.20]$) at Planta Río Cali — El Niño suppresses extreme daily precipitation — is consistent with orographic dynamics documented for the

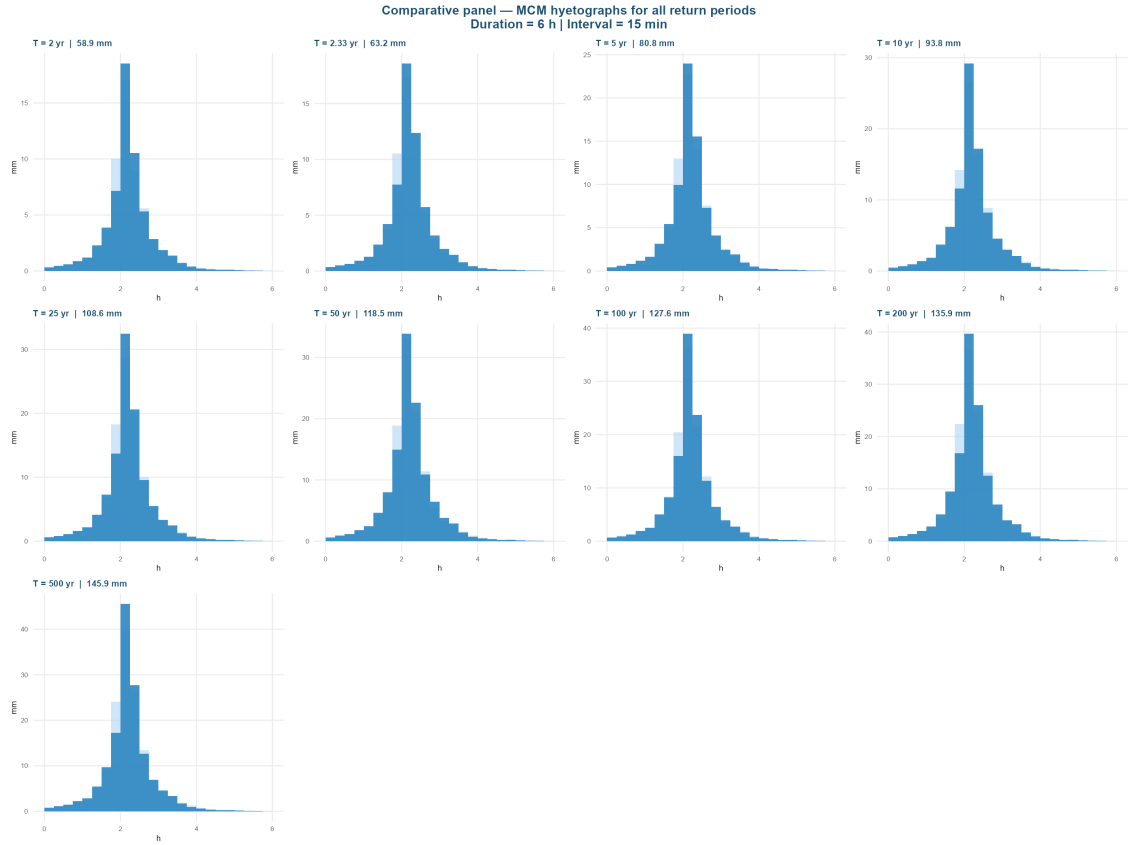

Figure 8: Comparative panel: MCM Q50 design hyetographs for all nine return periods (6-hour storm, $\Delta t = 15$ min, $n = 500$ realisations). Light blue: Q90 uncertainty band; dark blue: Q50 median. Total depths: 58.9 mm ($T = 2$ yr) to 145.9 mm ($T = 500$ yr). All hyetographs peak at $t \approx 2.25$ h (Huff Q2, Andean urban default).

Table 11: Peak 15-min intensity (mm h^{-1}) by ensemble percentile ($n = 500$, $\Delta t = 15$ min, `mcm_seed` = 42). Values are obtained by multiplying the maximum 15-min precipitation depth (mm) per simulation by the conversion factor 60 min/15 min $= 4.0$ to express intensity in mm h^{-1}. The Q90/Q10 ratio (≈ 2.4–2.5) is stable across return periods.

T (yr)	Q10	Q25	Q50	Q75	Q90
2	50.32	64.09	80.95	103.21	122.87
2.33	54.56	65.04	81.06	106.76	130.37
5	70.06	84.33	106.60	136.31	166.94
10	80.06	95.81	119.72	153.87	194.37
25	96.26	118.77	148.70	186.39	230.57
50	103.56	126.58	155.51	200.25	247.34
100	107.52	134.70	171.86	217.59	268.6
200	122.02	145.75	183.43	232.24	284.41
500	130.64	155.30	188.04	242.99	290.69

Q10–Q90: percentiles of the 500-simulation ensemble (precipitation depth percentiles, not exceedance probabilities).

western Cauca Valley [22]. During warm ENSO phases, weakened Pacific moisture advection reduces the supply of precipitable water to westward-facing Andean slopes. The practical engineering consequence is a design-depth reduction of $\hat{\beta}_1 \times |\Delta\text{ONI}| \approx 4.4$ mm for each unit increase in annual mean ONI: at $T = 100$ yr the design depth ranges from 132.0 mm (La Niña, ONI$= -1$) to 123.2 mm (El Niño, ONI$= +1$), a spread of 8.8 mm or $\sim 7\%$ of the neutral design depth (Table 7).

This station-specific signal contrasts with the broadly cited La Niña wet-anomaly narrative for Colombia, underscoring the necessity of station-level calibration rather than regional assumptions. The GAMLSS framework encodes this local signal through $\hat{\beta}_1$ and would produce a positive coefficient at stations on the eastern slopes of the Cordillera Central or in the Magdalena Valley where ENSO relationships are reversed [13]. Regionalisation of $\hat{\beta}_1$ across the CVC monitoring network would allow mapping ENSO-driven design-depth uncertainty across the Valle del Cauca.

5.2 Robustness of the majority-vote approach

The ensemble vote (4/6) demonstrates the inadequacy of relying on the MK test alone ($\tau = 0.0004$, $p = 1.0$): this would incorrectly classify the series as stationary. The complementary tests detect the structural break (Pettitt), localised trends (MWMK), and stochastic non-stationarity (ADF) that are invisible to a global monotonic trend test. This is precisely the situation predicted by [5] and [33] for series with regime changes superimposed on weak long-term drift — common in bimodal Andean climates [13].

The three strong votes (Pettitt, Sneyers, MWMK) carry more diagnostic weight than the weak ADF vote, as discussed in Section 3.1. Even discounting the ADF, the remaining 3/5 strong-test votes would satisfy the majority rule, providing robustness to this distinction.

5.3 The 2013 change-point and its implications

The Pettitt change-point at 2013 ($U = 600$, $p = 0.005$) is statistically robust but has an important caveat: only 11 years of post-break data are available. This is insufficient for independent sub-period GEV fitting, but this is not what the GAMLSS model does: it uses the *full* 71-year record, with ONI as a continuous covariate that accounts for year-to-year climate variability without requiring the series to be split. The change-point test therefore serves diagnostically — confirming structural non-stationarity — while the GAMLSS model provides the statistically sound inferential framework.

5.4 The CV_{ens} magnitude and its engineering meaning

CV_{ens} in the range 72–77% is substantially higher than values reported in studies where the MCM is calibrated from hourly data (∼20–40%, [20]). This difference directly quantifies the cost of the daily-to-sub-hourly scale extrapolation: calibrating at the monthly Pmax scale (∼24 h) and applying at 15-min intervals spans approximately $\log_{10}(1440/15) \approx 2$ orders of magnitude. The cascade has no information about the *shape* of precipitation within a day, only its daily total. The high ensemble spread does not make the results useless — the Q50 provides the expected temporal structure and the Q90 provides a conservative bound — but it does mean that the hyetographs should be interpreted as stochastic ensembles rather than deterministic design storms. For critical infrastructure design ($T \geq 100$ yr), the Q90 peak intensity (268.6 mm h^{-1} at $T = 100$ yr) is the appropriate design input. Local recalibration with CVC automatic stations would reduce CV_{ens} to operationally acceptable levels.

5.5 Comparison with deterministic methods

Two established deterministic methods are widely used in Colombian practice and are briefly described here for context before comparison. The *Chicago method* [6] constructs a synthetic hyetograph by differentiating an IDF relationship with respect to duration, producing a storm that reaches any given intensity with the frequency implied by the IDF curve; its temporal shape is controlled by a *peak coefficient* $r_{\text{Chicago}} \in [0, 1]$ that positions the peak within the storm duration. The *alternating blocks method* [7] distributes IDF intensities for sequentially shorter durations in an alternating pattern about the storm centre,

producing a symmetric hyetograph by construction. Both methods require a fixed IDF relationship and produce a single deterministic output.

The present MCM framework differs in three key respects:

- *Magnitude:* Non-stationary GAMLSS quantiles reflect the local ENSO-conditioned climate signal; regional atlases aggregate multiple stations under stationarity assumptions.
- *Uncertainty:* The MCM ensemble explicitly quantifies disaggregation uncertainty. Chicago and alternating blocks provide a single deterministic output with no uncertainty information.
- *Temporal structure:* The Huff quartile can be objectively determined from local data via r (Table 4), replacing the arbitrary r_{Chicago} (typically fixed at 0.4–0.5 based on temperate North American climatology — inappropriate for the Andean convective regime).
- *Reproducibility:* `MCM_Hyetographs` v1.0.0 is fully open-source with a centralised CONFIG section and automated outputs, enabling direct audit and replication.

5.6 Limitations

1. *Scale extrapolation:* MCM Beta parameters are calibrated at the daily Pmax scale and applied at 15-min intervals — a ratio of $1440/15 = 96$ ($\log_{10}(96) \approx 2$ orders of magnitude from the 24-h calibration anchor to the target 15-min step). This is the primary driver of the high CV_{ens}. Local automatic rain-gauge records would eliminate this extrapolation.
2. *ONI covariate: annual vs. seasonal aggregation:* Annual mean ONI smooths out the seasonal phase of ENSO teleconnections. A seasonally stratified covariate (e.g. ONI averaged over the local wet season, MAM or SON) would provide stronger physical coupling but at the cost of halving the effective covariate sample. This trade-off is acceptable for a 71-year record but should be revisited with longer or denser datasets.
3. *Single covariate and overfitting risk:* With $n = 71$ and one covariate, the GAMLSS model is parsimonious. Adding further covariates (AMO, PDO, SST) would require formal model selection (AIC comparison, regularisation) to avoid overfitting. No cross-validation was performed; leave-one-out or block-cross-validation is recommended before operational deployment.
4. *Return period interpretation under non-stationarity:* As noted by [25] and [8], the classical return period loses its strict probability-of-exceedance meaning when the distribution is time-varying. Design quantiles in Table 6 should be interpreted as conditional on the neutral ONI state, i.e., as expected waiting times under current climate.
5. *Post-break data limitation:* The 2013 change-point leaves only 11 years in the new regime. While the GAMLSS model handles this gracefully through continuous covariate modelling, the estimated $\hat{\beta}_1$ should be revisited as the record extends.
6. *Single-station case study:* Regionalisation of MCM parameters and ONI slopes across the CVC network is required before this methodology can be applied to ungauged catchments.

6 Conclusions

This paper presented an integrated, reproducible framework for synthetic design hyetographs under non-stationary climate conditions, applied to 71 years of data from the Planta Río Cali station, Valle del Cauca, Colombia. Six principal conclusions emerge:

1. A majority-vote ensemble of six stationarity tests (4/6) correctly identifies the series as non-stationary, where a global MK test alone ($\tau = 0.0004$) would have failed to do so. Three strong-signal tests (Pettitt, Sneyers, MWMK) independently confirm non-stationarity; the Pettitt test locates a structural break at 2013 ($p = 0.005$). The serial independence of the annual series ($r_1 = -0.03$, $p = 0.79$) validates the rank-based tests without pre-whitening correction.

2. The GEV-GAMLSS model with ONI covariate is preferred over the stationary GEV by formal AIC comparison ($\Delta\text{AIC} = 5.14$). It captures a station-specific negative ENSO effect ($\hat{\beta}_1 = -4.41$ mm per ONI unit; 95 % CI: $[-8.62, -0.20]$), consistent with orographic suppression on the western Cauca Valley slopes. The neutral-scenario 100-year 24 h design depth is 127.6 mm; the corresponding cumulative exceedance probability over a 50-year design life is 39.5 %, rising to 63.4 % over 100 years.

3. The Bell (1969) IDF curves, anchored on station GEV quantiles with $r_{60} = 0.40$ ($f_{60} \approx 1.003$, Eq. 6), provide intensities of 114.6 mm h^{-1} at 15 min, $T = 100$ yr — directly traceable to local data. A sensitivity analysis over the regional range $r_{60} \in [0.38, 0.45]$ yields intensity variations of $-5\,\%$ to $+12.5\,\%$ (Table 8), substantially smaller than the MCM ensemble spread (Q90/Q10 ≈ 2.4).

4. The $P(1\text{h})/P(24\text{h})$ ratio (r_{60}) is the only regional parameter in the IDF method; its selection guidance (Table 3) covers the principal Colombian climate regions. Local computation from overlapping hourly–daily records is always preferred.

5. The coefficient of advance r (Eq. 10) provides an objective, data-driven criterion for Huff quartile selection (Table 4), replacing the arbitrary choice implicit in conventional methods. For this case study, Q2 was adopted as the Andean urban default in the absence of sub-hourly records.

6. The MCM ensemble ($n = 500$, `mcm_seed` = 42) yields hyetographs peaking at $t \approx 2.25$ h with Peak/P_{total} = 28–31 % stable across all return periods. The Q90/Q10 peak intensity ratio of ≈ 2.4 at all T explicitly quantifies the disaggregation uncertainty invisible to deterministic methods: the Q90 peak at $T = 100$ yr reaches 268.6 mm h^{-1}, 56 % above the Q50 (171.9 mm h^{-1}), and is the recommended design input for critical infrastructure.

Acknowledgements

The author thanks CVC (Dirección Técnica Ambiental – Grupo Recursos Hídricos) for the Planta Río Cali precipitation record, and NOAA CPC for the ONI dataset. No specific funding was received. `MCM_Hyetographs` v1.0.0 is released as open-source software (MIT licence) at https://github.com/MauricioVictoriaN/MCM_Hyetographs_v1.0.0.

Declaration of competing interests: None.

Data and code availability: Supplementary Material S1–S4; code also available at https://github.com/MauricioVictoriaN/MCM_Hyetographs_v1.0.0.

Supplementary Material

S1. `MCM_Hyetographs_v1.0.0.R` — Complete R script (∼2,590 lines), MIT licence. Available at https://github.com/MauricioVictoriaN/MCM_Hyetographs_v1.0.0. **Note:** results in this manuscript were obtained with `CONFIG$mcm_seed` = 42; this value is set in the published script. Re-runs with `mcm_seed` = `NULL` will yield stochastically equivalent but numerically distinct ensemble outputs.

S2. Input data — `Pmax_24h.xlsx` (Planta Río Cali, 1954–2024) and `ONI.xlsx` (NOAA CPC).

S3. Full output — `MCM_results.xlsx` (13 sheets), `HEC_HMS_hyetographs.xlsx` (9 sheets), `REPORT_MCM_Stationarity.REPORT_MCM_Hyetographs.txt`, 20 PNG figures (11 diagnostic + 9 individual hyetographs, one per return period).

S4. Version history — v1.0.0: initial release (May 2026); v1.0.0 with seed 42: archived alongside this manuscript (June 2026).

S5. Monte Carlo convergence curves (Figure S1) — Q50 and Q90 of the peak 15-min depth as a function of n ($n = 50,\ 100,\ 200,\ 300,\ 400,\ 500$) for all nine return periods, confirming stabilisation within $\pm 2\,\%$ at $n \approx 300$.

S6. GAMLSS residual diagnostics (Figure S2) — Normalised-quantile Q-Q plot and worm plot [2] for the GEV-GAMLSS model. Shapiro-Wilk test on normalised residuals: $W = 0.975$, $p = 0.162$ (not rejected).

References

[1] Bell, F.C. (1969). Generalized rainfall-duration-frequency relationships. *Journal of the Hydraulics Division, ASCE*, 95(1), 311–327.

[2] van Buuren, S. & Fredriks, M. (2001). Worm plot: a simple diagnostic device for modelling growth reference curves. *Statistics in Medicine*, 20(8), 1259–1277. doi:10.1002/sim.746

[3] Burnham, K.P. & Anderson, D.R. (2002). *Model Selection and Multimodel Inference: A Practical Information-Theoretic Approach*, 2nd edn. Springer, New York. doi:10.1007/b97636

[4] Cai, W., Santoso, A., Collins, M., et al. (2021). Changing El Niño–Southern Oscillation in a warming climate. *Nature Reviews Earth & Environment*, 2, 628–644. doi:10.1038/s43017-021-00199-z

[5] Cheng, L., AghaKouchak, A., Gilleland, E. & Katz, R.W. (2014). Non-stationary extreme value analysis in a changing climate. *Climatic Change*, 127(2), 353–369. doi:10.1007/s10584-014-1254-5

[6] Keifer, C.J. & Chu, H.H. (1957). Synthetic storm pattern for drainage design. *Journal of the Hydraulics Division, ASCE*, 83(4), 1–25.

[7] Chow, V.T., Maidment, D.R. & Mays, L.W. (1988). *Applied Hydrology*. McGraw-Hill, New York. ISBN: 978-0-07-010810-3.

[8] Cooley, D. (2013). Return periods and return levels under climate change. In: AghaKouchak, A. et al. (Eds.), *Extremes in a Changing Climate*. Springer, Dordrecht. doi:10.1007/978-94-007-4479-0_4

[9] CVC (2025). Red de Monitoreo Hidrometeorológico del Valle del Cauca. Dirección Técnica Ambiental – Grupo Recursos Hídricos. Corporación Autónoma Regional del Valle del Cauca, Cali, Colombia.

[10] Delignette-Muller, M.L. & Dutang, C. (2015). fitdistrplus: An R package for fitting distributions. *Journal of Statistical Software*, 64(4), 1–34. doi:10.18637/jss.v064.i04

[11] Dickey, D.A. & Fuller, W.A. (1979). Distribution of the estimators for autoregressive time series with a unit root. *Journal of the American Statistical Association*, 74(366), 427–431. doi:10.2307/2286348

[12] Dunn, P.K. & Smyth, G.K. (1996). Randomized quantile residuals. *Journal of Computational and Graphical Statistics*, 5(3), 236–244. doi:10.2307/1390802

[13] Poveda, G. & Mesa, O.J. (1997). Feedbacks between hydrological processes in tropical South America and large-scale ocean–atmospheric phenomena. *Journal of Climate*, 10(10), 2690–2702. doi:10.1175/1520-0442(1997)010<2690:FBHPIT>2.0.CO;2

[14] Hingray, B. & Ben Haha, M. (2005). Statistical performances of various deterministic and stochastic models for rainfall series disaggregation. *Atmospheric Research*, 77(1–4), 169–185. doi:10.1016/j.atmosres.2004.10.023

[15] Huff, F.A. (1967). Time distribution of rainfall in heavy storms. *Water Resources Research*, 3(4), 1007–1019. doi:10.1029/WR003i004p01007

[16] IDEAM (2014). *Estudio Nacional del Agua 2014*. Instituto de Hidrología, Meteorología y Estudios Ambientales. Bogotá, Colombia.

[17] IPCC (2021). *Climate Change 2021: The Physical Science Basis*. Cambridge University Press. doi:10.1017/9781009157896

[18] Kendall, M.G. (1975). *Rank Correlation Methods*, 4th edn. Charles Griffin, London.

[19] Mann, H.B. (1945). Nonparametric tests against trend. *Econometrica*, 13(3), 245–259. doi:10.2307/1907187

[20] Molnar, P. & Burlando, P. (2005). Preservation of rainfall properties in stochastic disaggregation by a simple random cascade model. *Atmospheric Research*, 77(1–4), 137–151. doi:10.1016/j.atmosres.2004.10.024

[21] Pettitt, A.N. (1979). A non-parametric approach to the change-point problem. *Journal of the Royal Statistical Society: Series C*, 28(2), 126–135. doi:10.2307/2346729

[22] Poveda, G., Jaramillo, L. & Vallejo, L.F. (2014). Seasonal precipitation patterns along pathways of South American low-level jets and aerial rivers. *Water Resources Research*, 50(1), 98–118. doi:10.1002/2013WR014087

[23] Rigby, R.A. & Stasinopoulos, D.M. (2005). Generalized additive models for location, scale and shape. *Journal of the Royal Statistical Society: Series C*, 54(3), 507–554. doi:10.1111/j.1467-9876.2005.00510.x

[24] RAS (2010). *Reglamento Técnico del Sector de Agua Potable y Saneamiento Básico — Título D: Sistemas de Recoleccion y Evacuación de Aguas Residuales Domesticas y Aguas Lluvias*. Ministerio de Vivienda, Ciudad y Territorio. Bogotá, Colombia. Resolution 0330 of 2017 (update).

[25] Salas, J.D. & Obeysekera, J. (2014). Revisiting the concepts of return period and risk for nonstationary hydrologic extreme events. *Journal of Hydrologic Engineering*, 19(3), 554–568. doi:10.1061/(ASCE)HE.1943-5584.0000820

[26] Schertzer, D. & Lovejoy, S. (1987). Physical modeling and analysis of rain and clouds by anisotropic scaling multiplicative processes. *Journal of Geophysical Research*, 92(D8), 9693–9714. doi:10.1029/JD092iD08p09693

[27] Sneyers, R. (1990). *On the Statistical Analysis of Series of Observations*. WMO Technical Note No. 143. World Meteorological Organization, Geneva.

[28] Stedinger, J.R., Vogel, R.M. & Foufoula-Georgiou, E. (1993). Frequency analysis of extreme events. In: Maidment, D. (Ed.), *Handbook of Hydrology*. McGraw-Hill, New York. Chapter 18.

[29] Stephenson, A.G. (2002). evd: Extreme value distributions. *R News*, 2(2), 31–32. URL: https://CRAN.R-project.org/doc/Rnews/Rnews_2002-2.pdf

[30] Victoria Niño, M.J. (2026). Design storm duration from hourly rainfall records in a bimodal Andean climate. *EngrXiv* (preprint). doi:10.31224/7062

[31] Vélez, J.J., Botero, A. & Ramiŕez, A. (2002). Curvas de intensidad, duración y frecuencia para Colombia: ajuste de las relaciones IDF a registros pluviográficos. *Avances en Recursos Hidráulicos*, 9, 25–38.

[32] Vargas, R. & Díaz-Granados, M. (1998). Curvas sintéticas regionalizadas de intensidad-duración-frecuencia para Colombia. In *XIII Seminario de Hidráulica e Hidrología*, Sociedad Colombiana de Ingenieros. Cali, agosto 1998.

[33] Villarini, G., Smith, J.A., Serinaldi, F., Bales, J., Bates, P.D. & Krajewski, W.F. (2009). Flood frequency analysis for nonstationary annual peak records in an urban drainage basin. *Advances in Water Resources*, 32(8), 1255–1266. doi:10.1016/j.advwatres.2009.05.003

[34] White, H. (1980). A heteroskedasticity-consistent covariance matrix estimator and a direct test for heteroskedasticity. *Econometrica*, 48(4), 817–838. doi:10.2307/1912934

[35] Yue, S. & Wang, C. (2004). The Mann-Kendall test modified by effective sample size to detect trend in serially correlated hydrological series. *Water Resources Management*, 18(3), 201–218. doi:10.1023/B:WARM.0000043140.61082.60

[36] Yue, S. & Pilon, P. (2004). A comparison of the power of the t test, Mann-Kendall and bootstrap tests for trend detection. *Hydrological Sciences Journal*, 49(1), 21–37. doi:10.1623/hysj.49.1.21.53996

[37] WMO (2008). *Guide to Hydrological Practices, Volume I*, 6th edn. WMO-No. 168. World Meteorological Organization, Geneva. ISBN: 978-92-63-10168-6.